Article

Experimental Feasibility Study of a Direct Contact Latent Heat Storage Using an Ester as a Bio-Based Storage Material

Lukas Hegner †, **Stefan Krimmel, Rebecca Ravotti, Dominic Festini, Jörg Worlitschek** and **Anastasia Stamatiou** *

Competence Centre Thermal Energy Storage (CCTES), Lucerne University of Applied Sciences and Arts, 6048 Horw, Switzerland; hegnerl@ethz.ch (L.H.); stefan.krimmel@hslu.ch (S.K.); rebecca.ravotti@hslu.ch (R.R.); dominic.festini@gmx.ch (D.F.); joerg.worlitschek@hslu.ch (J.W.)
* Correspondence: anastasia.stamatiou@hslu.ch
† Current address: ETH Zürich, 8092 Zurich, Switzerland.

Abstract: Latent heat storage (LHS) represents a valuable technology for the integration of intermittent renewable energy sources in existing and future energy systems. Improvements in LHS can be sought by enhancing heat transfer efficiency, compactness and diminishing the environmental impact of storage systems. In this paper, direct contact latent heat storage (DC-LHS) using esters as phase change material (PCM) is proposed as a promising compact storage technology to achieve high performance both in terms of heat transfer and sustainability. The technology allows for the heat transfer fluid (HTF) to flow directly through the PCM, forming a large amount of small droplets and thus providing a large heat exchange surface area between the two materials. At the same time, using biobased esters as PCM, gives the technology clear ecological advantages when compared to alternative types of compact energy storage. Furthermore, no complex heat transfer enhancing structures are necessary in a DC-LHS, further reducing the environmental impact and enabling very high energy densities. In this paper, the feasibility of this concept is explored for the first time by developing and testing an experimental DC-LHS device using methyl palmitate as PCM and water as HTF. The thermal performance and stability of the material combination are analysed by different melting–solidification experiments and distinctive effects are identified and comprehensively discussed for the first time. The basic concept as well as the novel material combination are validated. The study finds the critical challenges that must be overcome in order for this highly promising technology to be successfully implemented.

Keywords: thermal energy storage; direct contact; latent heat storage; esters; methyl palmitate; phase change materials; PCM; proof-of-concept; emulsion

1. Introduction

Thermal energy storage (TES) could play a key role in energy transition, as it will allow for easy and environmentally friendly integration of renewable energy technologies in the energy sector. At the moment, in the context of renewable energy integration, energy storage is often synonymous to electro-chemical batteries. However, it is known that more than 90% of the world's primary energy generation is consumed or wasted in the form of heat or cold [1]. Additionally, it is becoming increasingly apparent that thermal energy storage can be successfully used also in applications typically associated with the use of batteries, like for the increase of self-consumption in residential photovoltaic (PV) systems. It has been demonstrated, for example, that a conventional TES can provide a similar degree of self-consumption and solar shares as battery storage in residential PV applications with half the installation costs [1]. Apart from the economical reasons, also ecological reasons point to the utilization of TES for applications where the energy is consumed in the form of heat or cold. Studies have shown that Li-ion batteries present serious environmental,

health and safety hazards and do not consist a sustainable storage solution at their present form [2,3].

Amongst TES technologies, latent heat storage (LHS), that is TES containing phase change material (PCM), is particularly interesting [4–9]. This is because of their high energy densities and constant charging and discharging temperatures. The operating principle of PCM is to undergo phase change during cycling and thereby store/release their phase change enthalpy. The ability to store large quantities of thermal energy in small volumes and narrow temperature ranges makes them ideal for applications where space is limited and/or that require temperature constancy. Some interesting implementations of PCM technologies exist in: heating and cooling of buildings [10,11], increasing thermal inertia of building components [12], smart textiles [8], temperature control industrial processes, in electronics and batteries [8,13,14].

Although the usage of PCM in TES has numerous advantages over sensible storage technologies, utilizing phase change also poses some challenges. Due to PCM's inherently low thermal conductivity [15], specially designed, complex structures are needed to enable fast charging/high thermal power over the entire cycle [16–20] which can often be costly and result in an energy density reduction. Direct contact latent heat storage (DC-LHS) can provide solutions to the mentioned limitations. It allows the flow of Heat Transfer Fluid (HTF) directly through the PCM without any barrier between the two immiscible substances. A density difference between the two components causes the HTF to pass through the PCM while the PCM remains in place. As the HTF passes through the PCM as a dispersed group of droplets, it releases/absorbs heat, causing the PCM to melt/solidify. The optimal proportion of PCM in the storage tank depends on the design and operating point of the system and is the subject of current research. However, DC-LHS can contain a proportionally large amount of PCM resulting in very high energy densities. Additionally, having a multitude of small HTF droplets passing through the storage tank generates a large heat-exchange surface area at the interface of HTF and PCM. This can give rise to high thermal powers [21]. The effect of this on heat transfer and the dominant mechanisms involved are subject of the research project to which this study belongs. Limited research has been reported on DC-LHS. The existing literature includes mostly experimental and limited modelling work [22]. Small laboratory setups have been developed and tested for specific combinations of PCM/HTF. The PCM/HTF material combinations tested include: (i) salt hydrates/oil [23,24], (ii) paraffin/water solutions [22], (iii) water/oil [25], (iv) erythritol/oil [26,27] and (v) ice/refrigerants [28]. Most studies have focused on cooling rather than heating applications [28]. The studies indicate a clear potential of the system, to achieve very high heat transfer rates. Additionally, supercooling and phase segregation during the crystallization of salt hydrates can be reportedly reduced, as the HTF bubbles passing through the storage volume agitate the PCM [29]. A uniform flow distribution improves heat transfer efficiency. Nozzle geometry and distribution have a major impact on this flow uniformity [30] and can prevent the formation of undesired dead zones [26]. The importance of flow control was also reported by Nomura et al. [26], in order to control residence time and flow uniformity.

When it comes to sustainability considerations, LHS can present many advantages both in terms of environmental impact as well as safety if a suitable PCM is chosen. In this study, carboxylic esters are selected as a particularly promising PCM in combination with the direct contact concept. Carboxylic esters are organic substances which present zero to low toxicity, low corrosiveness [31] and can be encountered in natural sources (e.g., in fats and fatty oils) [32,33]. As they are biobased, they do not contribute to depletion of natural resources while at the same time they can also act as carbon sequestrators [34]. A major obstacle for their widespread implementation is that many esters are not commercially available or are produced in very low quantities and are therefore too expensive to be realistically considered for latent storage applications. However, the fact that some of the most established esters are very cost-efficient (e.g., methyl palmitate) and companies are emerging that supply exclusively bio-based PCM at prices comparable to those of

paraffins (e.g., CrodaTherm products), combined with the foreseen growth of the market for nature-based energy solutions, it is expected that the economies of scale will enable many bio-based esters to become available in the future at competitive prices. Carboxylic esters present good thermal properties and a wide spread of melting temperatures [31,35–39]. There are thousands of esters that could be potentially used as PCM but their properties remain unknown. Fatty esters are the most investigated class of esters in the context of PCM [40–42]. Up to now, esters have been mostly investigated on the material level and very limited results have been presented regarding their operating in LHS systems. If their combination with DC-LHS proves to be successful, they could allow for the creation of a compact energy storage system that is entirely nature-based (excluding the storage tank) and could therefore be a crucial development for a sustainable energy future. To the authors' knowledge no DC-LHS system using esters has been developed or investigated to this point.

This study aims to assess the feasibility of using a combination of fatty acid esters (PCM) and water (HTF) in the DC-LHS context which is a rather complex, highly-stochastic system and subject to material-specific challenges. The research questions were defined as follows: (i) Material stability: are the chosen materials thermally stable and chemically inert under the chosen operating conditions? (ii) Operational stability: Is it possible to run a full charging and discharging cycle and close the energy balance (store and extract the theoretically calculated amount of heat)? Under which experimental conditions is a stable operation possible? What are the factors that contribute to unstable operation (e.g., blockage or contamination of the system)? Are the experiments repeatable or is the level of stochasticity too high and/or the impact of externalities too great? (iii) Thermal performance: How is the measured power profile connected to the observed structures formed during solidification/melting? How sensitive is the performance of this unoptimized system to the nozzle design and inlet temperature of the HTF? In addition to being the first time a direct contact proof-of-concept setup was created using an ester as PCM, to the best of the authors knowledge, this is also the first study that clearly presents the biofouling challenge as well as an analysis and detailed discussion of the emulsification issue.

2. State of the Art

Despite their high potential, several challenges have been identified that hinder the stable operation of direct-contact systems. The formation of solid PCM channels around the inlet nozzles, which obstruct the HTF flow, have been observed. Flow 'dead zones' within the solidification space cause low heat transfer rates [22]. Direct-contact interactions of organic compounds, especially with water, could potentially lead to changes in the chemical composition of components and can bring about biofouling [43]. PCM carry-over from the storage tank into the HTF cycle causes blockages in pipes and can damage equipment when the PCM solidifies [44].

PCM carry over can occur via different mechanisms. The issue has been known since the early days of the direct contact technology [44] where increased carry over was correlated to higher viscosity PCM. Other sources in the literature mention that PCM carry over can occur as a consequence of the swelling of liquid PCM during charging [22] or can be caused by the formation of solid PCM layers around HTF bubbles [45,46]. Over the course of this investigation, PCM carry over was observed as a result of (i) a fine dispersion of PCM in HTF, where the dispersed droplets/particles were so small that they followed the HTF flow and were not separated by the difference in density as desired and (ii) the buildup of an emulsion (liquid–liquid dispersion) of HTF in PCM at the PCM–HTF interface that grew large enough to be sucked into the HTF piping. This foam-like emulsion at the interface between PCM and HTF will from now on be referred to as the 'bulk' emulsion. Despite their big influence on system performance, very little reporting and almost no analysis of this phenomenon is present in literature. The fine dispersion will most likely have been the cause of carry over in the investigations of Edie et al. [44], while the 'bulk' emulsion has been reported and documented to a certain extent by Nogami et al. [23]. The

build-up of this PCM 'bulk' emulsion is due to the slow coalescence of the PCM droplets as additional bubbles arrive at the PCM–HTF interface. A solution to the 'fine' emulsion type, for water in oil emulsions, was proposed by Ammann et al. [47] using a superhydrophobic sponge filter. The problem linked to solidified PCM around HTF bubbles has been tackled before by adding perforated partition plates to the storage tank [45] and more recently with use of aluminium fibres in the solidification space that were able to break these PCM covered bubbles [48]. Despite the lack of extensive analysis of these effects in the context of thermal energy storage, similar phenomena have been extensively reported and analysed in other fields. The determination of coalescence profiles and parameters of liquid–liquid dispersions have been of interest and investigated for some time as they represent important processes used for solvent extraction in industry [49–51].

Biofouling has not been reported in the context of direct contact thermal energy storage before. However, it has been observed by the authors in several direct contact systems investigated in-house including the one analysed in the present study. It is believed to further promote the emulsification mechanism causing the 'bulk' emulsion. As such, it causes increased difficulties and represents a major barrier to the further advancement of this technology. Biofouling is a phenomenon well known in the fuel storage industry [43]. The most frequently reported microbe contamination in fuel storage is *Hormoconis resinae*, known commonly as 'diesel bug' or 'kerosene fungus', however there are many different bacteria and fungi that grow in fuel storage tanks [52]. Fungi and other microorganisms consume the fuel and cause it to degrade, with hydrocarbons of linear structure being more vulnerable to biodegredation than their branched isomers [53]. The microorganisms thrive in the presence of water with most growth occurring at the fuel/water interface. It is common to find communities living within slimy layers called biofilms that may exist on tank walls, the tank roof or the interface between the fuel and water [53].

3. Materials and Methods

3.1. Materials

All experiments were carried out using methyl palmitate, a fatty acid methyl ester, as PCM. Deionised water served as HTF in all experiments. The methyl palmitate was purchased from Sigma Aldrich (St. Louis, MO, USA) with purity ≥97% and used without further purification.

3.2. Measurement of Methyl Palmitate Meterial Properties and Stability

The phase change temperature and enthalpy of fusion of the PCM were determined with differential scanning calorimetry (DSC 823e, METTLER TOLEDO, Columbus, Ohio, USA) using the methodology described by Ravotti et al. [31]. The mentioned thermal properties were determined by melting and solidifying three different samples six times at heating rates of first $10\,\mathrm{K\,min^{-1}}$ to determine the phase change enthalpy then $2\,\mathrm{K\,min^{-1}}$ to determine the melting and crystallization points. The values reported are the mean of the measured values. As the methods are clearly described in the aforementioned reference, they are not further explained hereby. The PCM phase change temperature, used in all experiments, was determined to be 29 °C which is consistent with the literature value [31].

The thermal stability of methyl palmitate (absence of degradation when exposed to thermal stress) as well as its chemical stability (absence of reaction with water and other surrounding materials) were assessed by comparing the melting enthalpy of PCM samples before and after the cycling and emulsification experiments. The comparison was based on DSC measurements of (i) the unused PCM, and (ii) three PCM samples taken from different locations in the glass tube after the end of the experimental campaign (mean value of enthalpies was used). It is worth mentioning, that the experimental campaign was conducted over the course of 3 months. If the difference in the measured enthalpy before and after the cycles was less than the measurement error of 3.5% (as stated by the manufacturer [54]), the material was considered thermally and chemically stable under these operating conditions.

3.3. Experimental Setup

The test rig consists of the direct contact storage tank and the infrastructure required to operate it (see Figure 1). The direct contact storage is comprised of a 1 m long, square glass tube of dimensions 50 mm × 50 mm which stores the PCM and through which the HTF flows in the direction of gravity. The glass tube allows for optical access and is oriented vertically to ensure symmetric flow conditions inside the tube. The inlet nozzle is a 6 mm steel tube which is inserted into the glass tube through a GL45 fitting seen on the right in Figure 1. The glass tube is filled with 1 L PCM and 1.1 L HTF, which corresponds to a height of 90 cm from the bottom during operation. The 1 L of PCM was measured at 20 K above PCM melting temperature.
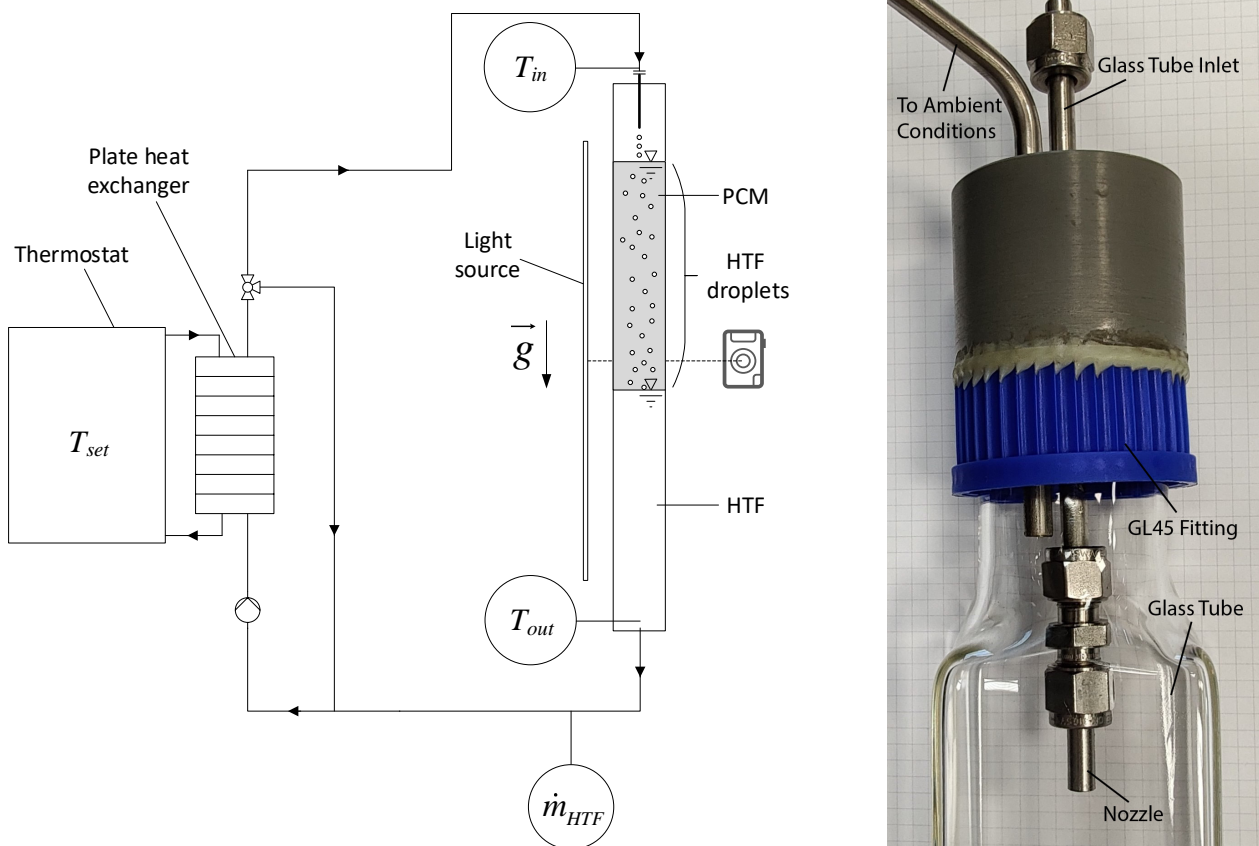
Figure 1. (**Left**) Schematic of the experimental setup. From the bottom left in direction of the HTF flow one can see: the pump, the plate heat exchanger and thermostat, the three way ball valve connected to the glass tube inlet and the bypass. Following the HTF toward the glass tube, the inlet temperature can be seen being measured immediately before the nozzle. The glass tube, seen on the right in the figure represent the tank, contains the PCM and HTF. Images are taken of the process in the glass tube using a camera and a light source. The outlet temperature is measured immediately before the glass tube exit. The mass flow is measured using an ultrasonic flow meter, before the HTF flow from the glass tube is rejoined by the HTF from the bypass. (**Right**) Close up of GL45 fitting and the top of the glass tube, in this case with the short nozzle attached.

The remaining infrastructure is connected to the storage tank via the inlet and outlet. A gear pump delivers the HTF through a plate heat exchanger to the three-way valve at the inlet of the glass tube. The plate heat exchanger is connected to a thermostat, which allows HTF temperature regulation. The three way valve at the inlet of the direct contact storage can direct HTF through the glass tube and the PCM or the system bypass or both simultaneously. The bypass allows for more precise system operation at small mass flows and enabled the user to bring the HTF to the desired temperature before it was passed through the PCM. The HTF mass flow passing through the PCM was measured by a

ultrasonic flow meter placed immediately after the glass tube. The mass flow through the glass tube was actively adjusted by the PID controlled pump which received inputs from the users commands and the flow meter. The temperatures were measured at the inlet and outlet of the glass tube as well as outside the system boundaries to gauge the ambient temperature. The 1 mm Type-K thermocouples, were placed in the center of the HTF flow to measure the inlet and outlet temperatures while the ambient temperature was measured by a PT100 sensor. All data were logged by a National Instruments DAQ system with a sampling rate of 1 Hz and displayed in Labview in real time. Detailed information on the components used can be found in Table 1.

Table 1. Setup components overview.

Component	Manufacturer	Model	Comment
Pump	Marco	UP3 24V	Gear pump
Heat exchanger	unknown	Plate heat exchanger	12 Plates
Thermostat	Huber	CC505	-
Flow meter	Flownetix Ltd	100series	-
Thermocouple 1	thermocoax	Type2	1 mm type K mantle
Thermocouple 2	thermocoax	Type2	1 mm type K mantle
PT100 sensor	unknown	-	-
DAQ Chassis	National Instruments	NI cDAQ-9189	-
Temperature input module 1	National Instruments	NI-9216	PT100 input
Temperature input module 2	National Instruments	NI-9214	Thermocouple input
Glass tube	Hofmann Glastechnik GmbH	Custom tube	$1000 \times 50 \times 50$ mm
Insulation	Armaflex	Armaflex/HT	-
Fittings	Swagelok	-	Stainless steel
Camera	Sony	Alpha 600	24.3 Megapixel

Before initial experiments, all sensors and measuring chains were calibrated. The temperature sensors were calibrated by comparison measurement with a reference sensor. The comparative measurement was carried out in a homogeneous temperature field of a water glycol mixture at support points -10 °C, 0 °C, 10 °C, 20 °C, 25 °C, 30 °C, 50 °C, 55 °C, 70 °C and 90 °C. The temperature range of the experiments to be carried out was covered completely by the calibration temperatures. The reference sensor can be traced back to the ITS90 of ± 0.02 K according to certificate number 2018-1253 of the accredited calibration laboratory (accreditation number SCS 0066) of mcs laboratory AG, 6460 Altdorf, Switzerland. The mass flow sensor was calibrated over a series connection with a coriolis flow meter. The targeted massflow rates were 20 kg h^{-1}, 30 kg h^{-1}, 40 kg h^{-1} and 50 kg h^{-1} at temperatures 5 °C, 25 °C, 45 °C and 75 °C to investigate the measurement dependence on mass flow and temperature.Armaflex/HT of thickness 10 mm was used to insulate the pipes leading from the thermostat to the glass tube inlet. The glass tube itself was left without insulation for most experiments as optical access was of interest. Three melting/solidification cycles were carried out with an insulated glass tube to investigate the influence of externalities on thermal performance. As no significant difference between the insulated and uninsulated system was found, as can be seen in Figure 2, the results presented in this paper stem from uninsulated experiments for which optical access was available. Figure 2 shows raw data of inlet and outlet temperature measurements of two melting processes, where all other experimental parameters apart from insulation type were kept the same. For one of the two cycles, Cycle 13, the glass tube was completely insulated with the same Armaflex HT material used to insulated the pipes. The data of Cycle 7, the other data shown in the plot, were obtained with an uninsulated glass tube. The plotted curves display very similar profiles and show that the influence of insulation is only minor.
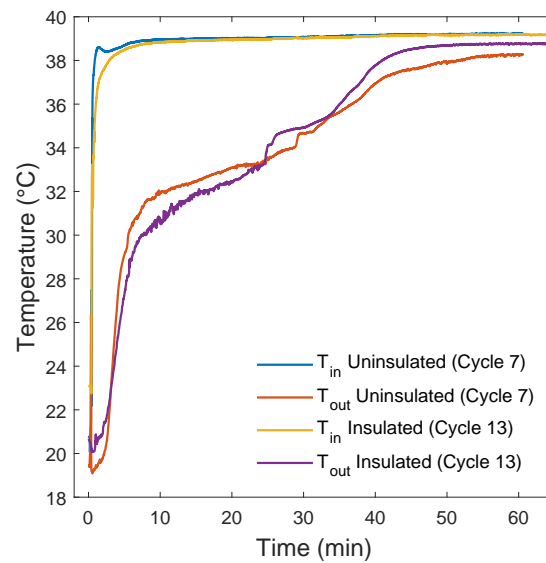
Figure 2. Comparison between the temperature profile of an uninsulated and an insulated melting process. The inlet temperatures are shown in yellow for the insulated case and in blue for the uninsulated case, while the outlet temperature is shown in purple for the insulated measurements and red for the uninsulated data.

The entire setup, bar the thermostat, was additionally completely covered by a plastic sheet that reached the laboratory floor to minimise influence of forced convection and ensure similar temperature conditions throughout the vicinity of the glass tube. The plastic sheet also prevented any external light to reach the glass tube, preventing heating through radiation and improving image quality when taking pictures. Images were taken of experiments, whenever optical access was available, using a Sony alpha600 24.3 megapixel camera, (Minato City, Tokyo, Japan). The camera was mounted at a distance of 60 cm to the stored PCM and was focused to capture the developments inside the glass tube. To improve image quality, the PCM in the glass tube was back-lit using a diffused LED strip. A paper-strip with 5 mm thickness, equally spaced, black and white lines, was mounted between the light source and the glass tube to provide a reference scale bar, facilitate comparison between images and improve contrast. In experiments that ran for extended periods of time, such as melting/solidification experiments or emulsion growth rate investigations, the camera system was triggered every 5 s by the labview program. For the melting/solidification tests specifically, the LED light source was not running permanently but was also triggered simultaneously with the camera as to minimise thermal influence of radiation.

A nozzle was used to direct the HTF flow vertically downwards into the PCM placed in the center of the glass tube. This allowed for symmetrical flow conditions inside the glass tube. Before the overall parameter study was initiated, some preliminary experiments were carried out. Over the course of these preliminary tests, two nozzle designs were considered and tested. The first design had the nozzle, a stainless steel pipe of diameter 6 mm, immersed 7 cm in the PCM while the second nozzle design consisted of a shorter steel pipe of the same diameter which reached to 8 cm above PCM level surface at 10 K above PCM melting temperature. The second design forced the HTF to pass through empty space before reaching the PCM. Ultimately, the short nozzle design was chosen and all of the PCM melting–solidification experiments as well as the emulsion buildup tests were carried out making use of this design.

3.4. Experimental Methods

3.4.1. Cleaning the System

As system contamination, in the form of biofouling or PCM carry over, was observed on several occasions, an adequate method of cleaning the system had to be developed. Since the glass tube allowed for visual inspection of system cleanliness, it was possible to clearly identify when the system needed to be cleaned. Isopropanol was used to clean the inside of the glass tube between PCM changes, when the biofouling problem became substantial (when the biofilm grew higher than 2 mm). To clean the glass tube, it was removed completely from the setup to allow for better access. The inside of the tube was scrubbed and isopropanol was applied again until the tube was clean. If there was any indication of PCM carry over into the HTF piping, the remaining piping was rinsed with hot tap water at high mass flow rates for extended periods of time up to 40 min. The system was always rinsed before adding new PCM by filling it with deionised water and pumping several different, medium-high mass flows. The rinse water was then emptied and fresh deionised water was filled into the system. This ensured prolonged periods of clean system operation before the biofouling appeared again in substantial quantities. However, small quantities of biomaterial was often seen soon after the PCM was added to the setup, even though the pipes and heat exchanger were cleaned and rinsed thoroughly beforehand.

3.4.2. Heat Loss Experiments

To determine the energy stored by the system, it was necessary to quantify the heat losses of the system to the surroundings. The heat loss experiments were carried out with the system filled to the top of the glass tube with HTF, without any PCM. The heat losses of the system in the liquid phase, with a completely full glass tube represent the maximum possible heat losses.

A range of mass flows from $18.2 \, \mathrm{kg \, h^{-1}}$ to $43 \, \mathrm{kg \, h^{-1}}$ and temperatures from $19 \, °\mathrm{C}$ to $44 \, °\mathrm{C}$ were targeted to completely cover any experimental parameters later chosen. The entire range of tested mass flows and temperatures were measured for both an insulated and uninsulated system. These experiments resulted in a heat loss function for both configurations of the system.

3.4.3. Emulsion Buildup Characterization

The preliminary experiments made clear that the setup had some limitations in terms of the maximum energy-storing rate. The presented system allowed for a maximum mass flow rate of $18.2 \, \mathrm{kg \, h^{-1}}$. One of the limiting factors revealed itself as a "bulk" emulsion of HTF bubbles and PCM at the interface of the two substances. If the buildup of this bulk emulsion increased too much it would cause a large amount of PCM carry over into the HTF piping. Such emulsions, sometimes called "foams" or "droplet accumulation" have been mentioned in research before. Nogami et al. even mention undesired PCM carry over as a result of this emulsion buildup [23]. PCM carry over is to be avoided at all cost as it could result in a system blockage during the solidification process. As understanding emulsion buildup is necessary for dimensioning and safe optimisation of such direct contact storage systems or for developing a methodology to avoid the emulsification altogether, a separate study of parameters, investigating this phenomenon, was carried out. Additionally, the results of this study defined the safe operating parameters for the melting–solidification experiments.

For all experiments there was 1 L of PCM (at 20 K above PCM melting temperature) with a mass of of 856.5 g in the system. This resulted in a volume ratio of around 10:11 PCM to HTF inside the glass tube, a volume ratio of around 10:15 PCM to HTF in the overall system (including the piping). Defining a volumetric quantity of PCM rather than a mass allows for the same geometric proportions of PCM to HTF in case the PCM is changed in other experiments. The geometric proportions will influence the structure of the solid PCM matrix in solidification experiments as well as the emulsion height. All of the emulsion buildup experiments were carried out with the system being in the

liquid–liquid configuration, without the presence of solid PCM or PCM solidification. A range of different mass flows (15 kg h^{-1}, 18.2 kg h^{-1}, 19.1 kg h^{-1}, 20 kg h^{-1}, 25 kg h^{-1} and 30 kg h^{-1}) was targeted at 10 K above PCM melting temperature to investigate the influence of mass flow rate on the emulsion height. The emulsion height was measured, using a ruler, from the first layer of emulsified HTF bubbles, to the point where the HTF bubbles coalesce back into the HTF, stored in the glass tube. This can be seen in Figure 3.
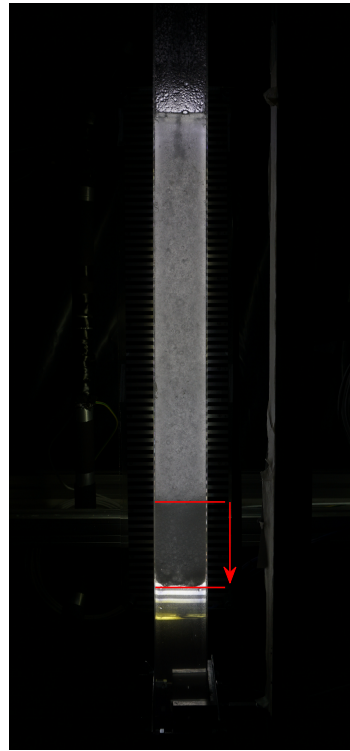

Figure 3. Measurement of the emulsion height. In the upper section of the glass tube a multiphase flow of HTF through PCM can be seen. In the middle section the 'bulk' emulsion to be measured can be seen (indicated by the red arrow). A layer of HTF is visible below the 'bulk' emulsion.

In a few experiments the biofilm would visually noticeably wrap around the emulsion buildup. This is further discussed in Section 5. The emulsion was measured to the point where the regime of the homogeneously sized bubbles ends. The HTF wrapped in biocontamination would not be measured as part of the emulsion height. The height of the emulsion was measured after the emulsion growth had stopped and the system had reached steady state (when no emulsion growth was recorded over 5 min). To prevent PCM carryover, the experiment would also have to be stopped when the emulsion of a certain mass flow rate had surpassed the maximum allowable level. The set mass flow rates was targeted one after another from the lowest mass flow (15 kg h^{-1}) to the highest mass flow (30 kg h^{-1}).

3.4.4. Melting-Solidification Experiments

To determine thermodynamic properties of the storage system, melting/solidification experiments were carried out. The experiments also gave an indication of PCM cycling stability within the direct contact system and would reveal any unforeseen difficulties of using methyl palmitate as a direct contact PCM. The camera setup was used to record the melting and solidification process.

To investigate the influence of HTF temperature on PCM melting/solidification behaviour, tests were carried out at a HTF temperature difference of 10 K and 5 K to PCM melting temperature. The experiments carried out to study the effect of insulation were carried out at a HTF temperature difference of 10 K to PCM melting temperature as a greater temperature difference to ambient conditions would amplify the measured effect of the insulation. All melting–solidification experiments were carried out using the same mass flow of 18.2 kg h^{-1}. The emulsion buildup investigation had shown, that a mass flow of 18.2 kg h^{-1} would allow for safe operation of the system and initial solidification test showed that this held true during solidification also. A higher mass flow rate could have potentially resulted in PCM carry over as the PCM solidified.

The methodology, to investigate the melting and solidification behavior of the system, involved a melting process followed by a solidification process. Both the melting and solidification processes were carried out at same temperature difference to the PCM melting temperature. Since the solidified PCM would approach room temperature after an experiment was concluded, in order to gain comparable data, the system needed to be cooled to the required temperature before a new melting process could be initiated. The system was cooled by passing cold HTF through the solid PCM structure. It was important that the solid PCM matrix, from an earlier experiment, was formed under the same conditions (same HTF inlet temperature) as the experiment to be carried out. The solidification temperature could influence the structure of the PCM matrix which could potentially influence the melting rate. It was sometimes necessary to perform additional solidification cycles that could not be analysed as to begin the melting measurements with the correct solid PCM matrix. Once the temperature difference between the HTF at the inlet and the outlet was constant, the mass flow was stopped, the three way valve was adjusted to close off the glass tube (leaving only the bypass open) and the thermostat was set to the temperature that was used to melt the PCM. Once the thermostat had reached the desired temperature, the pump was started to heat the HTF in the bypass. Having preheated the HTF in the bypass, the three way valve was adjusted to allow HTF flow through the glass tube. The PID controller would adjust the HTF mass flow passing through the glass tube to the set value. The system was left running until all the PCM had melted and the difference between the inlet and outlet temperature became constant. When the steady state was reached, the mass flow was stopped. For the examination of the solidification process, the same experimental procedure was followed with the HTF temperature set below PCM melting temperature. Once the PCM had solidified completely and a steady state temperature-difference between the inlet and outlet was reached, the experiment was terminated. To assess the repeatability of the experiments, each melting/solidification process was repeated three times. Table 2 lists the melting–solidification experiments carried out. The measurement of the methyl palmitate material properties was carried out before the initial melting–solidification experiment and again after the final melting–solidification experiment. All of the melting–solidification experiments were carried out using the shorter nozzle.

Table 2. Experimental matrix of the melting–solidification experiments carried out.

Experiment Title	Experiment Presented	Date	Melting Temperature	Solidification Temperature	Insulation	Nozzle Type
Cycle 1	No	15 January 2020	44 °C (+15 K)	19 °C (−10 K)	No	short
Cycle 2	No	16 January 2020	44 °C (+15 K)	19 °C (−10 K)	No	short
Cycle 3	No	17 January 2020	44 °C (+15 K)	19 °C (−10 K)	No	short
Cycle 4	No	29 January 2020	44 °C (+15 K)	19 °C (−10 K)	No	short
Cycle 5	**Yes**	**31 January 2020**	**39 °C (+10 K)**	**19 °C (−10 K)**	**No**	**short**
Cycle 6	**Yes**	**31 January 2020**	**39 °C (+10 K)**	**19 °C (−10 K)**	**No**	**short**
Cycle 7	**Yes**	**1 Feruary 2020**	**39 °C (+10 K)**	**19 °C (−10 K)**	**No**	**short**
Cycle 8	No	10 Feruary 2020	34 °C (+5 K)	24 °C (−5 K)	No	short
Cycle 9	**Yes**	**10 Feruary 2020**	**34 °C (+5 K)**	**24 °C (−5 K)**	**No**	**short**
Cycle 10	**Yes**	**11 Feruary 2020**	**34 °C (+5 K)**	**24 °C (−5 K)**	**No**	**short**
Cycle 11	**Yes**	**11 Feruary 2020**	**34 °C (+5 K)**	**24 °C (−5 K)**	**No**	**short**
Cycle 12	No	17 Feruary 2020	39 °C (+10 K)	19 °C (−10 K)	Yes	short
Cycle 13	**Yes**	**17 Feruary 2020**	**39 °C (+10 K)**	**19 °C (−10 K)**	**Yes**	**short**
Cycle 14	**Yes**	**18 Feruary 2020**	**39 °C (+10 K)**	**19 °C (−10 K)**	**Yes**	**short**
Cycle 15	**Yes**	**18 Feruary 2020**	**39 °C (+10 K)**	**19 °C (−10 K)**	**Yes**	**short**
Cycle 16	No	12 March 2020	39 °C (+10 K)	19 °C (−10 K)	Yes	short
Cycle 17	No	12 March 2020	39 °C (+10 K)	19 °C (−10 K)	Yes	short

3.5. Calculations

3.5.1. Energy Balance

For the calculations of the thermal performance, the beginning and end of a cycle was defined. Melting and solidification were regarded separately and the start of each process was defined as the beginning of the HTF mass flow through the glass tube. A melting or solidification process would be considered complete when system steady state was observed (the gradient of the outlet temperature being below $0.03 \, \mathrm{K \, s^{-1}}$). The thermodynamic system boundary was drawn around the outside of the glass tube. The enthalpy flow into the system was calculated as the difference between inlet and outlet temperature multiplied by the mass flow rate and c_p value of the HTF.

$$\Delta \dot{H}_{htf} = \dot{m}_{htf} \cdot c_{p,htf} \cdot (T_{in} - T_{out}) \tag{1}$$

The heat losses of the system to the environment were approximated by a calibration function developed using the method described in Section 3.4.2. The function was determined experimentally and was fitted on a polynomial with the parameters seen below. It gives the system heat losses for specific conditions of HTF mass flow and temperature difference between the ambient conditions and the system.

$$\dot{Q}_{loss} = f(\dot{m}_{htf}, T_{system} - T_{ambient}) \tag{2}$$

All melting/solidification experiments were carried out at a HTF mass flow of $18.2 \, \mathrm{kg \, h^{-1}}$, resulting in a heat loss function dependent only on temperature. The outlet temperature gave the best approximation of the system temperature from the measurements available and was assumed to be equal to system temperature in calculations. The system boundaries were defined as shown in Figure 4 and the heat stored by the system over time, $\frac{dE}{dt}$, was calculated by subtracting the heat losses from the HTF enthalpy flow into the system.

$$\dot{Q}_{charge} = \frac{dE}{dt} \tag{3}$$

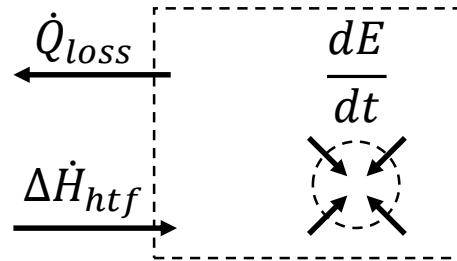$$\frac{dE}{dt} = \Delta\dot{H}_{htf} - \dot{Q}_{loss} \tag{4}$$

Figure 4. Schematic of the system boundaries and energy flows. The arrows indicate the direction of the heat flow during a melting process with the system above room temperature.

The degree of charge or "load" was calculated by the integration of the stored heat over time and dividing by the total amount of energy the system could potentially store denoted Q_{max}. Due to limitations of the experimental setup, it was no possible to distinguish between the multiple simultaneously active heat sources and heat sinks. Since no distinction between the different heat storages (e.g., PCM, HTF in the glass tube, glass tube) was possible, Q_{max} includes the HTF inside the glass tube as well as the glass tube itself. The material properties of the glass tube were taken from the suppliers data sheet [55]. Q_{max} was calculated using the difference in system temperature between the first and final measurement. This means that the sensible heat, stored before and after phase change, is included when considering the maximum storable energy. All of the PCM was assumed to have undergone a complete phase change resulting in Equation (5).

$$Q_{max} = m_{pcm} \cdot h_{melt} + \left[m_{pcm} \cdot c_{p,pcm} + m_{htf} \cdot c_{p,htf} + m_{glass} \cdot c_{p,glass} \right] \cdot \left[T_{out}(end) - T_{out}(begin) \right] \tag{5}$$

To determine the amount of heat actually stored in the system, the store rate was integrated over charging/discharging time. Since the beginning and end of charging/discharging was defined as the start and stop of HTF flow through the storage, Q_{store} also includes the sensible heat stored by the system. The chosen method of integration is shown in Equation (6) as a summation of the individual heat flow measurements.

$$Q_{store} = \sum_{t_{begin}}^{t_{end}} \left\{ \dot{Q}_{charge}(t) \cdot \Delta t \right\}; \qquad \begin{cases} Q_{store} > 0 : & \text{melting} \\ Q_{store} < 0 : & \text{solidification} \end{cases} \tag{6}$$

The load, of both melting and solidification, is calculated as:

$$Load = \frac{Q_{store}}{Q_{max}} \tag{7}$$

3.5.2. Error Propagation

Table 3 shows the approximated measurement uncertainties that were used in calculations.

Table 3. The uncertainties used in measurement error analysis.

Value	Absolute Uncertainty	Relative Uncertainty
m_{pcm} = 0.8565 (kg)	δm_{pcm} = ±0.005 (kg)	±0.584%
h_{melt} = 210,130 (J/kg)	δh_{melt} = ±21,013 (J/(kgK))	±10%
$c_{p,pcm}$ = 1960 (J/(kgK))	$\delta c_{p,pcm}$ = ±196 (J/(kgK))	±10%
m_{htf} = 1.1 (kg)	δm_{htf} = ±0.05 (kg)	±5%
$c_{p,htf}$ = 4228 (J/(kgK)) [56]	$\delta c_{p,htf}$ = ±6 (J/(kgK))	±1.4‰
m_{glass} = 1.603 (kg)	δm_{glass} = ±0.1 (g)	±0.01%
$c_{p,glass}$ = 800 (J/(kgK))	$\delta C_{p,glass}$ = ±40 (J/(kgK))	±5%
T_{out} (K)	δT_{out} = ±0.03 (K)	
T_{in} (K)	δT_{in} = ±0.03 (K)	
$\Delta T_{in,out} = T_{in} - T_{out}$ (K)	$\delta(\Delta T_{in,out})$ = ±0.01 (K)	
$\dot{m}_{htf}$ (kg/s)	$\delta \dot{m}_{htf}$ = ±0.0083 (kg/s)	
$\dot{Q}_{loss}$ (J/s) (max = 22 J/s)	$\delta \dot{Q}_{loss}$ = ±− (J/s)	±20%

The measurement uncertainty in the enthalpy flow into the system could be calculated by assuming independent variables.

$$\delta \Delta \dot{H}_{htf} = \sqrt{\left(\frac{\partial \Delta \dot{H}_{htf}}{\partial \dot{m}_{htf}} \cdot \delta \dot{m}_{htf}\right)^2 + \left(\frac{\partial \Delta \dot{H}_{htf}}{\partial c_{p,htf}} \cdot \delta c_{p,htf}\right)^2 + \left(\frac{\partial \Delta \dot{H}_{htf}}{\partial(\Delta T_{in,out})} \cdot \delta(\Delta T_{in,out})\right)^2} \quad (8)$$

The uncertainty of the stored energy per time step could be calculated as follows using the same principles. Uncertainties are added in quadrature as can be seen in Equation (9) for a single time step:

$$\delta(\Delta \dot{H}_{htf}(t) - \dot{Q}_{loss}(t)) = \sqrt{(\delta \Delta \dot{H}_{htf}(t))^2 + (\delta \dot{Q}_{loss}(t))^2} \quad (9)$$

Because of the chosen method for integration introduced in Equation (6), and the measurement time step of 1 s, the uncertainty of the stored energy was calculated as follows.

$$\delta Q_{store} = \sqrt{\sum_{t_{begin}}^{t_{end}} (\delta \Delta \dot{H}_{htf}(t))^2 + (\delta \dot{Q}_{loss}(t))^2} \quad (10)$$

To be able to find the measurement uncertainty in the load, the uncertainty in Q_{max} was calculated. For the uncertainty propagation analysis the value of Q^*_{max} and its uncertainty were calculated as a theoretical value for each experiment. A distinction is made between the cycles run at a 5 K difference to the PCM melting temperature where: $\Delta T = |T_{out}(end) - T_{out}(begin)| = 10$ and the cycles run at a 10 K difference to the PCM melting temperature where: $\Delta T = 20$.

$$\underbrace{(m_{pcm}) \cdot (h_{melt}) + \left[(m_{pcm}) \cdot (c_{p\ pcm}) + (m_{htf}) \cdot (c_{p\ htf}) + (m_{Glass}) \cdot (c_{p\ Glass})\right] \cdot \left[\Delta T\right]}_{Q^*_{max}} \quad (11)$$

The uncertainty in the load was then calculated as:

$$\delta(Load) = Load \cdot \sqrt{\left(\frac{\delta Q_{store}}{Q_{store}}\right)^2 + \left(\frac{\delta Q^*_{max}}{Q^*_{max}}\right)^2} \quad (12)$$

4. Results

4.1. Effect of Nozzle Design

The preliminary investigation on the influence of nozzle design lead to the short nozzle being used in the great majority of experiments carried out. Initially, the design

of the longer nozzle, immersed in the PCM, seemed promising, as it would prevent air from being trapped in the solidifying PCM matrix and minimised unnecessary turbulence (thereby decreasing the emulsion buildup). However, upon PCM solidification, the even HTF inlet jet caused a solid PCM channel to form around the nozzle exit and prevented circulation of warm PCM in the upper regions of the glass tube shown in Figure 5. This channel ultimately lead to low heat transfer rates in this upper area of the storage and caused very long solidification times of up to several hours. Below this formed PCM channel, solidification continued normally as the HTF was able to disperse over the entire glass tube cross-section. In addition to the problem of channel-formation, the immersed nozzle is believed to have caused PCM carry over to the HTF cycle by allowing PCM to travel up the nozzle. The carry over was detected upon solidification, as the PCM began blocking the pipes. Another phenomenon documented while using the immersed nozzle was the growth of PCM up along the metal nozzle upon solidification. This is a phenomenon that has previously been observed with other PCM in other LHS and can be seen in Figure 6. In addition to the behaviour of the immersed nozzle, Figure 5 also shows the operational behaviour of the short nozzle, with which the increased turbulence at the Air–PCM interface prevented channel formation. This caused a different solidification phenomenon as it resulted in solid PCM flakes forming from bulk, falling to the PCM–HTF interface and accumulating there. The prevention of channel formation eliminates the dead space and poor heat transfer rates in the storage.
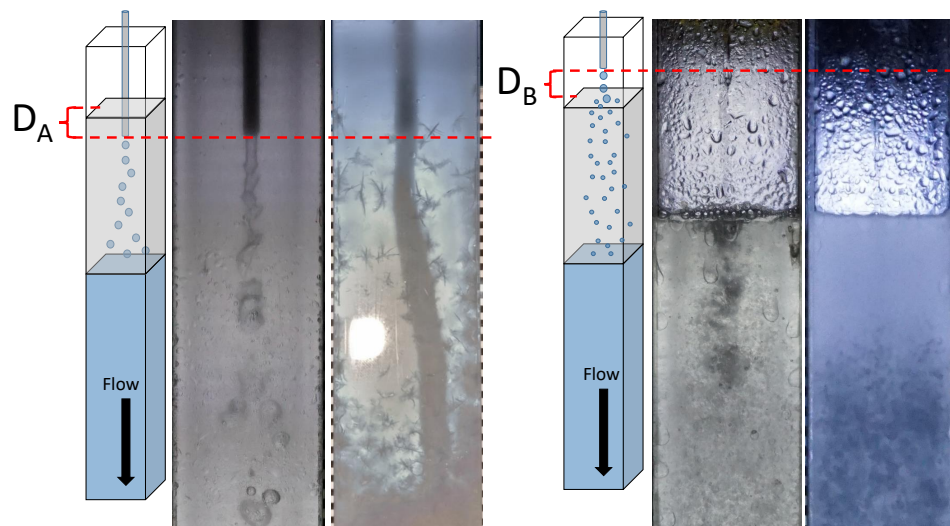

Figure 5. Two sets of images showing characteristic behaviour of the nozzle immersed into the PCM ($D_A = 7$ cm) in the image group on the left, and the short nozzle ending above the PCM ($D_B = 8$ cm) in the image group on the right. Both image sets show (1) a schematic of the nozzle design, (2) HTF flow of 23 kg h^{-1} (at 15 K above PCM melting temperature) into the PCM and (3) distinct solidification behaviour (18.2 kg h^{-1}; 10 K below PCM melting temperature) respectively. Limited turbulence and single channel formation can be seen with the immersed nozzle while increased turbulence, higher HTF-PCM surface area and flake formation is observed with the short nozzle.

No blockages have been observed with the short nozzle. However, a small amount of PCM carryover into the HTF cycle part of the system occurred nonetheless. As will be discussed, the shorter nozzle decreased the maximum allowable flow rate as the increase in turbulence caused greater bulk emulsion buildup at the interface between PCM and HTF. Even though the increased turbulence at the interface between HTF and PCM decreased the maximum allowable flow rate by the producing a larger bulk emulsion, the short nozzle also increased the HTF surface area exposed to the PCM as it produced smaller HTF bubbles.

Figure 6. PCM solidification along the immersed nozzle.

The discussed effects highlight the importance of nozzle design when building this type of direct-contact storage system. The two nozzles resulted in very different systems and had different advantages and drawbacks. All of the discussed results from this point onward were obtained with the short nozzle, as this nozzle was deemed more suitable for the planned application.

4.2. Methyl Palmitate Material Properties and Stability

Table 4 lists the material properties of methyl palmitate, measured as described in the methods section. The data presented in Table 4 were gathered before any experiments were carried out with the PCM.

Table 4. Initial, measured material properties of methyl palmitate.

Material	ρ (kg m^{-3})	c_p (J/(kgK))	h_{melt} ($\pm\sigma$) (kJ kg^{-1})
Methyl Palmitate (PCM) solid (10–29 °C)	-	1960	210.1 ($\pm$1.1)
Methyl Palmitate (PCM) liquid (29–59 °C)	846	1960	210.1 ($\pm$1.1)

To get an indication of PCM stability within the presented system, the melting enthalpy of the PCM was measured again after the 17 cycling experiments had been carried out. The mean melting enthalpy, determined by the same method, was 206.9 kJ kg^{-1} with a standard deviation of 3.2 kJ kg^{-1}. The drop in melting enthalpy from 210.1 kJ kg^{-1} to 206.9 kJ kg^{-1} is within the measurement error of 3.5%, stated in the handbook of the measurement equipment [54]. It could therefore be said that the PCM underwent only slight changes, if any, over the course of the experiments.

4.3. Emulsion Buildup Characterisation

The investigation of bulk emulsion height at different HTF mass flow rates and different system temperatures revealed some relevant factors that should be considered when operating the direct contact setup. As seems intuitive, greater HTF mass flow rate lead to a larger bulk emulsion height. This was shown to be true for all temperatures tested and was an effect that could be shown reproducibly. The initial bulk emulsion buildup tests were carried with new PCM in the system and can be seen in Figure 7 where the measured steady state emulsion height is plotted over the HTF mass flow.
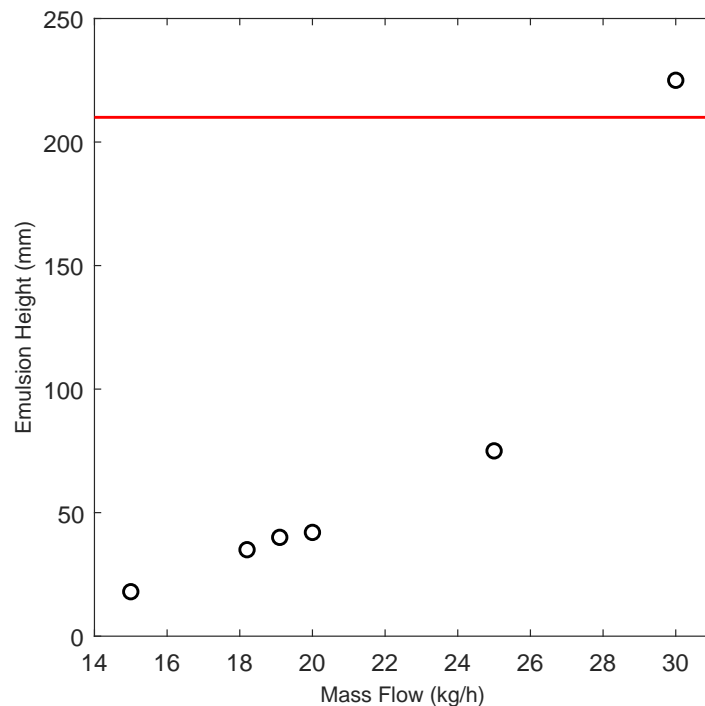
Figure 7. Data points of steady state emulsion heights recorded on the first day of the emulsion buildup investigation. The red line indicates the maximum allowable emulsion height before the experiment had to be terminated.

Very high mass flow rates would result in experiments having to be terminated as the emulsion would surpass a level of 210 mm. At emulsion heights above 210 mm there was a risk of the emulsion being sucked into the glass tube outlet in which case the test was terminated to prevent this. In Figure 7, this emulsion height limit can be seen as a red line. In the graph, the first five steady state data points show a linear increase of emulsion height with increased HTF mass flow rate. The sixth data point shows a measurement not taken at steady state as the experiment had to be terminated before such a steady state was reached.

Interestingly, many of the observed bulk emulsion effects could not be measured repeatedly. When steady state emulsion heights were measured on later dates with identical experimental parameters, larger values were recorded. Over the course of 6 days, the steady state emulsion height increased by over 400% for all tested mass flow and temperature settings. Figure 8 shows the emulsion buildup in steady state conditions on the 3rd day of the emulsion tests. Here the set experimental parameters (10 K above PCM melting temperature) are the same as for the data generated on day 1, however the measured heights have increased by over 100% for all mass flows.

It is believed that many different interacting effects cause this phenomenon. Some sort of system memory causes a greater emulsion buildup following stress imposed on the system on the same day and even from days before. It is theorised that an increase in biomaterial in the system contributed to the increase in steady state emulsion height however, this needs to be explored in a further study as it is not within the scope of this investigation. The biofilm, that accumulates at the PCM–HTF interface over time, is seen wrapping around the PCM covered HTF bubbles and increases emulsion stability. This further discussed in Section 5. The emulsion would only be measured to the point where the regime of the homogeneously sized bubbles ends. The HTF wrapped in biocontamination would not be measured as part of the emulsion height.
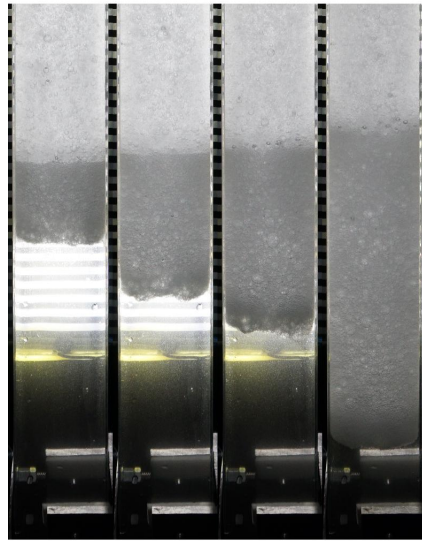
Figure 8. Images of the steady state emulsion height at 10 K above PCM melting temperature, recorded on day 3 of the emulsion buildup investigation. The mass flow settings of the images from left to right: 15 kg h^{-1}, 18.2 kg h^{-1}, 20 kg h^{-1}, 25 kg h^{-1}.

Overall it can be said that emulsion height increases linearly with HTF mass flow until a critical mass flow rate is reached and that steady state conditions exist below this critical value. Above this critical value, the emulsion increases steadily outside of the range measurable with the presented system. It was not possible to detect the influence of temperature on emulsion buildup with this system, possibly because of the dominant influence of other effects.

If PCM carry over from the storage tank to the rest of the system is to be avoided, the increase in bulk emulsion with an increase of HTF mass flow will limit the enthalpy flow through the PCM. As the direct contact technology has advantages that are useful in high power applications, which rely on fast charging and discharging rates to deliver high thermal powers, maximising the HTF mass flow will be desired in many cases. The use of demulsifiers should be investigated in upcoming studies, as a means to prevent the build-up of the bulk emulsion. This will a key development to ensure stable operation and successful implementation of direct contact TES in future applications.

4.4. Melting-Solidification Experiments

Figure 9 presents raw data gathered during a typical melting–solidification cycle. The chosen cycle (cycle 7), seen in Figure 9 and in the image sequence of Figure 10 was carried out with HTF temperatures set at 10 K above the PCM melting temperature (29 °C) for melting and 10 K below PCM melting temperature for solidification. The HTF inlet and outlet temperatures are shown in dark and light blue respectively and correlate to the left y-axis while the mass flow can be seen in orange and on the right hand y-axis. Both temperature data and mass flow measurement are plotted over experiment run time in minutes. The graph and image sequence should give insight into the melting and solidification experiments and some of their results.

Until point 1 of the graph in Figure 9, the system has been running on the low temperature setting and has reached the steady state temperature. The mass flow through the glass tube is stopped and the thermostat is set to the "high" temperature setting. No cold HTF passes though the PCM and the system begins approaching a higher ambient temperature. At point 2 the thermostat has reached the desired high temperature for melting and the HTF has been preheated in the bypass. Now the three way valve is turned, the mass flow passing through the glass tube is increased to 18.2 kg h^{-1} and the PCM begins to melt. A small overshoot in PID response of the pump can be seen. The inlet temperature shows the step response while the system begins to absorb heat from the HTF.

As can be seen in Figure 10, the PCM–HTF level begins to rise due to thermal expansion of the materials in the storage tank. For melting the characteristic phase change plateau is not well defined but a distinct gradient decrease can be seen in T_{out} as the PCM melts between points A and B in Figure 9. This decrease of the outlet temperature gradient is due to the latent heat being released as the PCM is melting. Point 3 shows fluctuations of the outlet temperature in the part of the graph influenced by latent enthalpy. As the solid PCM matrix melts, PCM that was held in place by the solid structure breaks free and moves toward the interface between PCM and HTF. The images of Figure 10 that correspond to point 3 were taken 5 s apart and show a block of PCM moving upwards rapidly.
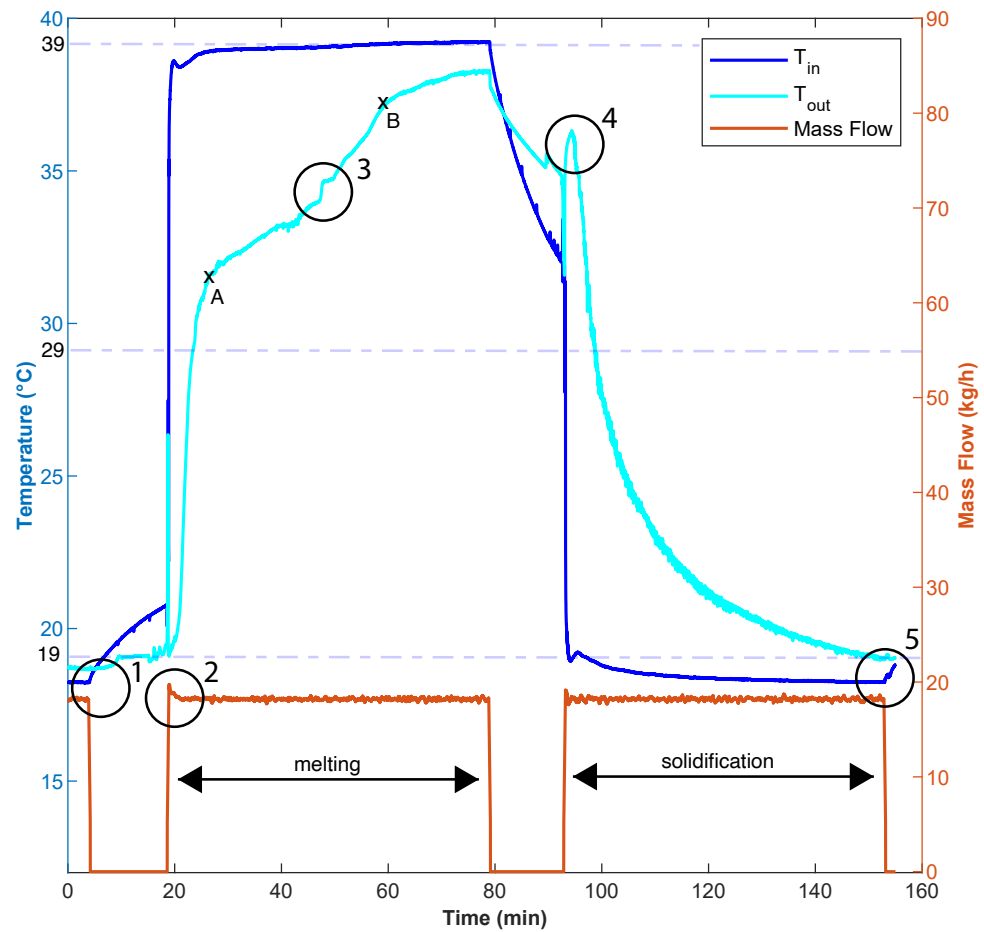

Figure 9. Temperature profile of Cycle 7. Inlet and outlet temperatures in °C are visible in blue (on the left hand y-axis), while mass flow in kilograms per hour is shown in orange (on the right hand y-axis). Experiment run time is shown in minutes and 5 points of interest are marked in the plot. Point 1 shows first stoppage of mass flow through the system to allow the thermostat to heat up. Point 2 shows the start of the melting process. Point 3 shows some temperature fluctuations, characteristic of this setup. The PCM melts between points A and B. Point 4 and Point 5 mark the beginning and end of the solidification process.

Such temperature fluctuations, caused by migration of solid PCM, were present in all of the cycles.

The HTF is pumped through the glass tube until all of the PCM has melted and the outlet temperature has reached equilibrium at minute 80 of the experiment. Again the mass flow through the glass tube is stopped as the thermostat is cooled to the chosen PCM-solidification temperature setting. At point 4 when the cold mass flow through the glass tube is re-initiated, the outlet temperature spikes as the stratified HTF stored in the glass tube passes the outlet temperature sensor. Solidification of PCM begins only seconds

after the HTF mass flow starts. No supercooling was identified in any of the experiments as the cold HTF stream always began solidification at the point where it made initial contact with the PCM. Crystals are formed from bulk in the vicinity below the HTF jet and are driven downwards by the HTF flow and gravity. This can be seen in the image corresponding to point 4 in Figure 10. Initially, the PCM crystals are remelted by the warm PCM surrounding them. After a minute of cold HTF passing through the glass tube, the flakes are no longer remelted and begin to accumulate at the HTF PCM interface. The PCM flakes that appear initially on solidification can also appear in the form of solidified PCM enclosing a HTF drop at a greater temperature difference between the HTF and PCM. This has previously been mentioned in literature [45,46].
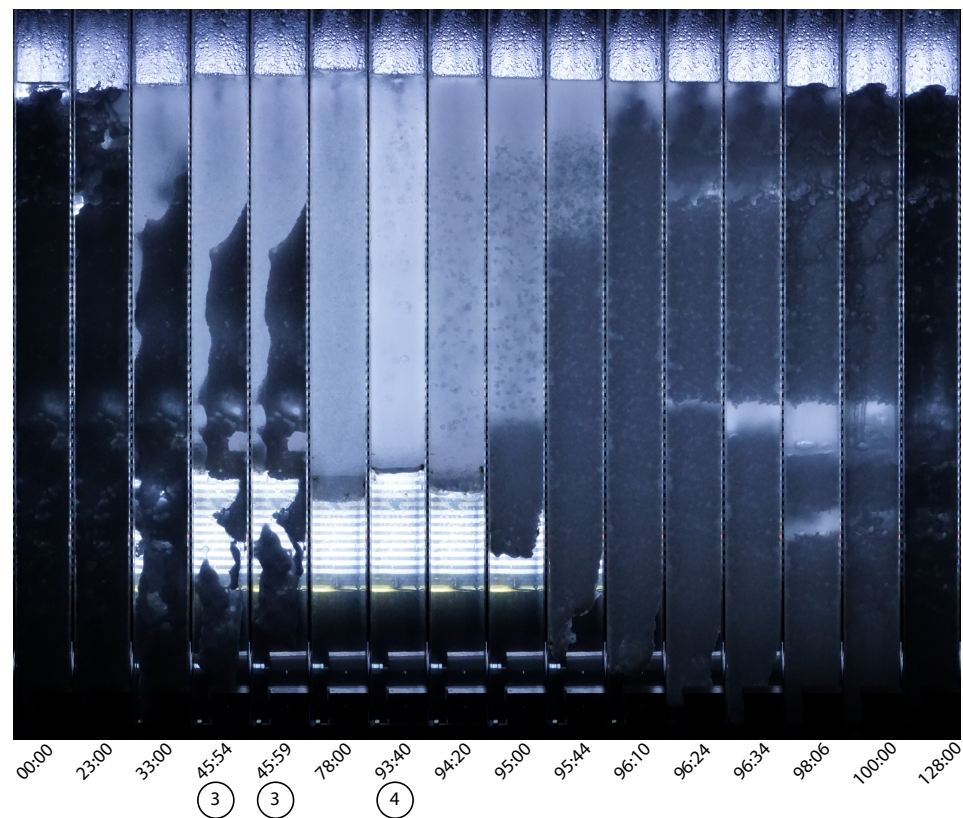

Figure 10. Image sequence of Cycle 7, corresponding to the temperature profile shown in Figure 9. The time stamps underneath the images are in the format: t = mm:ss. The PCM in can be seen melting and resolidifying over the course of 2 h. The numbers in circles underneath some of the images correspond to the points of interest marked in Figure 9.

This initial solid structure continues to grow from the PCM crystals accumulating above and is pushed further down into the HTF below. As the density of solid PCM is lower than that of the HTF, the PCM structure floats at the interface. The PCM structure encloses HTF droplets causing the volume taken up by the solid PCM to be much larger than that of the PCM in liquid state. After only 3 min of the solidification process, 80% of the glass tube is taken up by the PCM structure. When the solid PCM structure reaches the interface of the PCM with the air, cracks appear and the matrix is torn apart as can be seen at 96:24 in the image sequence. These separate PCM blocks travel down the glass tube and may even separate again. This effect was observed in every solidification experiment carried out. In contrast to the moving PCM block observed during melting, the movement of this solidifying structure is not noticeable in the thermal data. Once the blocks come to rest the liquid PCM between them solidifies slowly. The PCM becomes more dense as the system temperature decreases further. While the influence of the latent heat of the PCM is clearly visible during the melting process, the solidification temperature profile shows only

few signs of solidification. A sign of solidification can be seen as the slope of T_{out} which is less steep during solidification than during the initial stages of melting process. At point 5 the experiment is terminated as the outlet temperature has reached steady state.

The melting–solidification experiments proved to have high reproducibility considering the complexity and inherent stochasticity of the system. This can be seen in Figure 11 where three power ($\dot{Q}_{charge}$) profiles are overlaid in the same figure. All melting–solidification experiments were repeated three times to verify this. The best reproducibility was observed for the cycles that had additional insulation surrounding the glass tube. For the cycles in Figure 11, the peak power of the system during melting is between 406 W and 426 W and the melting process takes around an hour.
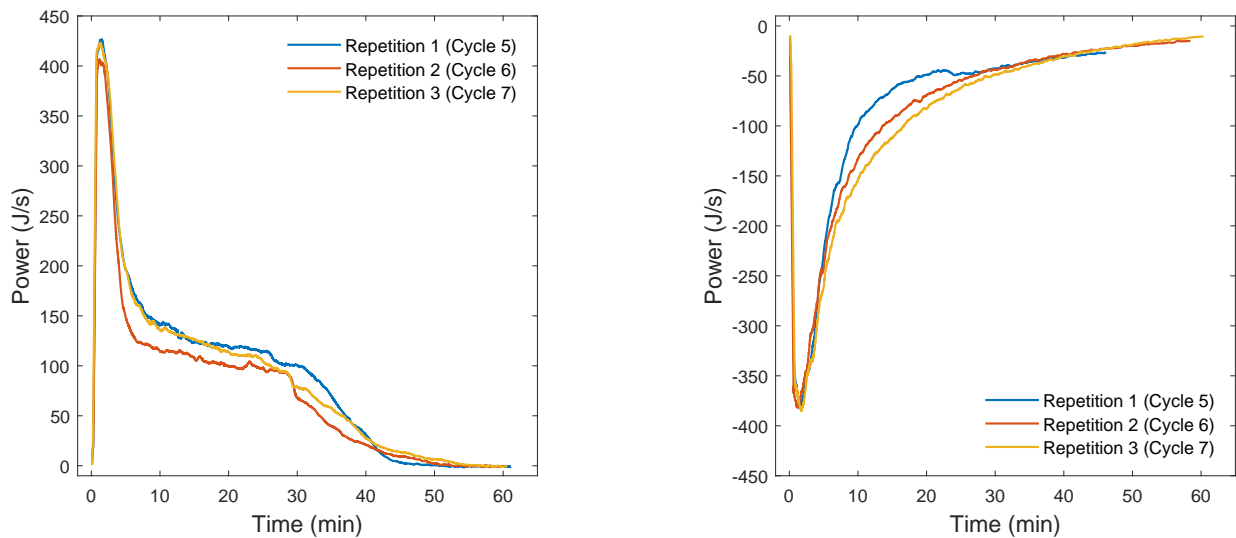

Figure 11. Power profiles ($\dot{Q}_{charge}$ over time) of 3 melting (**left**) and solidification (**right**) processes of the same experimental parameters, showing the reproducibility of experiments. Melting and solidification took place at 10 K above and below PCM melting temperature respectively at a mass flow of 18.2 kg h^{-1}. Cycle 5, Cycle 6 and Cycle 7 are shown.

The greatest deviation from a group of three repetitions was observed during the solidification process of Cycle 5, seen in Figure 11 as repetition 1 in blue. The deviation from the data set was determined to be due to the particular manner the PCM solidified as channel formation prevented a higher heat absorption rate from being achieved. At the point where the power curve of repetition 1 rejoins the other cycles, a piece of solid PCM was observed obstructing a previously open channel through the PCM matrix. It is assumed that this previously open channel, now closed, caused the HTF to pass through sections of the storage tank that still contained PCM at a higher temperature. The peak power of the system for solidification is 5–13% lower than that of the melting process with power peaks between −371 W and −385 W. This can be explained by the fact that the system loses more heat to the surroundings while waiting for the thermostat to reach the cold setting as the temperature difference to ambient conditions is larger at the beginning of the solidification process than at the beginning of the melting process.

The chosen HTF inlet temperatures and their difference to the phase change temperature play an important role in LHS system performance. To test the influence of this factor on the thermal behaviour of the setup, tests with HTF temperatures at 5 K above PCM melting temperature and 5 K below PCM melting temperature were also carried out and their reproducibility is shown in Figure 12. Very similar performance was observed with respect to the experiments with 10 K temperature difference. As expected, a lower peak and plateau power were measured which resulted to slightly longer overall charging/discharging times especially during the solidification process.
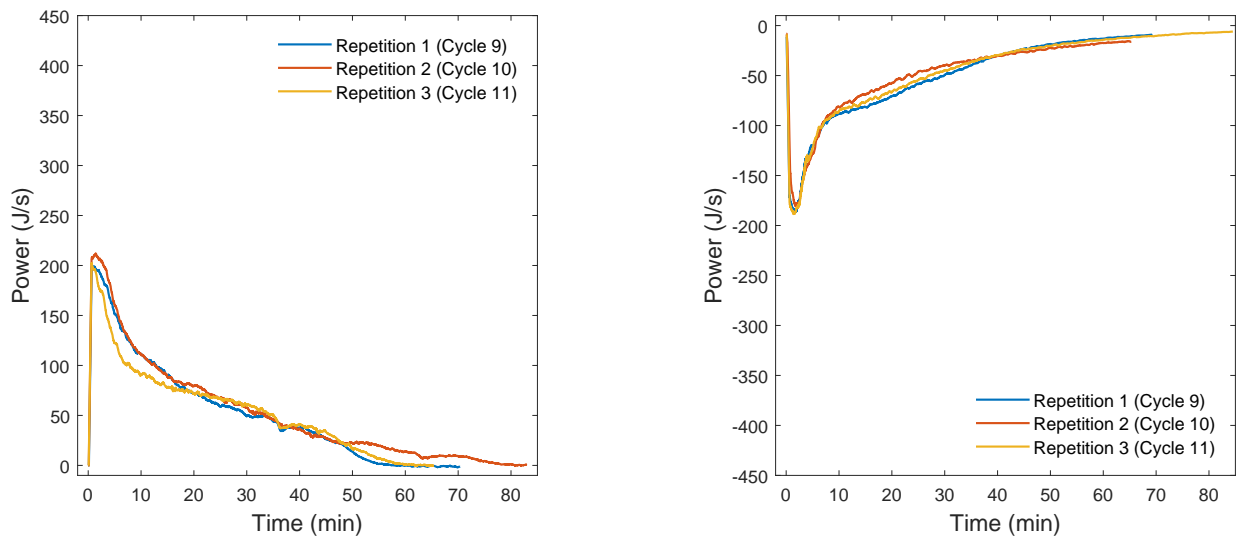
Figure 12. Power profiles ($\dot{Q}_{charge}$ over time) of 3 melting and solidification processes of the same experimental parameters, showing the reporducibility of experiments. Melting and solidification took place at 5 K above and below PCM melting temperature respectively at a mass flow of 18.2 kg h^{-1}. Cycle 9, Cycle 10 and Cycle 11 are shown.

Figure 13 shows the load as a function of time for both melting and solidification of Cycle 7. These calculations revealed that it was possible to charge and discharge the storage device fully, closing the energy balance. However, it can also be seen that there is a large measurement uncertainty (represented by the gray area in the graph) despite having accurate measurement equipment. This is due to the nature of the load calculation as the error reported in this case accounts for the sum of errors over the entire course of the experiments. Interestingly, despite the high uncertainty connected to the calculation of the heat losses (see Table 3), they proved to have no major influence on the overall uncertainty.
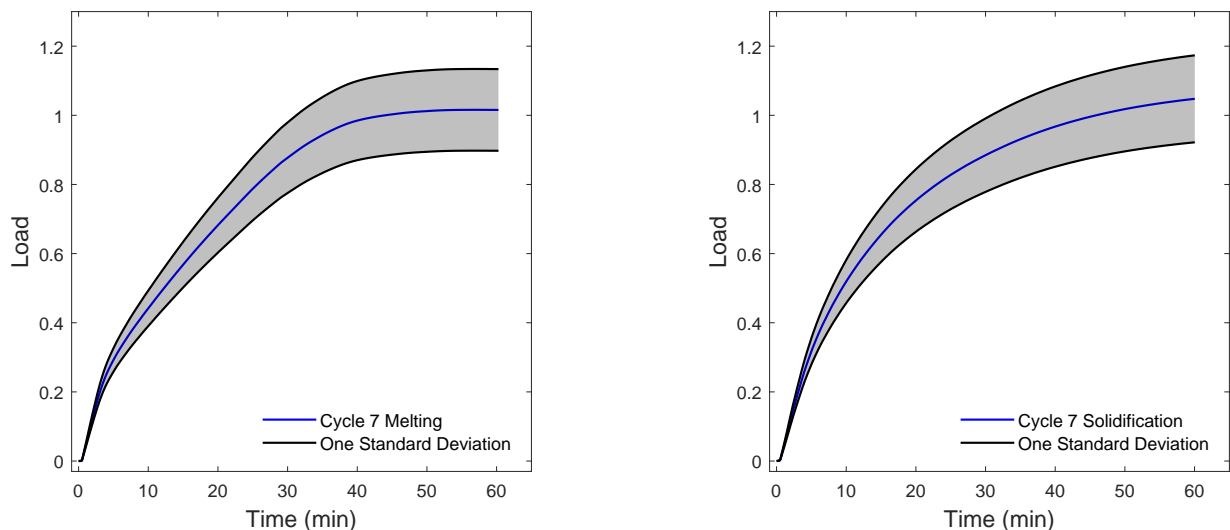

Figure 13. Load of melting (**left**) and solidification (**right**) of Cycle 7 shows the degree and rate of charge over the course of a cycle. The uncertainty of the measured value was calculated using Equation (12).

A power ($\dot{Q}_{charge}$) over load graph allows for comparison of processes with different run times. It is therefore suitable to compare the charging/discharging processes of experiments with different HTF inlet temperatures tested in this investigation. Figure 14 (left) shows the melting process and Figure 14 (right) the solidification process of two cycles with two different HTF inlet temperatures. Naturally the experiments with the 5 K setting (T_{in} = 34 °C for melting and 24 °C for solidification) have a much smaller peak power

than the 10 K experiments (T_{in} = 39 °C for melting and 19 °C for solidification) as there is less sensible heat stored in the system and less driving force for the heat transfer between the storage medium and the HTF. It is interesting to observe that for the melting process while the peak power of the +10 K is approximately double than that of the +5 K, the same doesn't hold for the plateau-power which is approximately 20–40% higher in the former case. The same tendency is also observed for the solidification even though the plateaus are much less pronounced. A relatively stable temperature and therefore power output during the largest part of the charging and discharging process is of course desired in most latent storage systems. The existence of rather short and not very clear plateaus hint to the formation of relatively few, big channels of HTF in the solidified PCM structure rather than a network of small, branched channels that would result to higher and more stable power outputs. This performance is expected to improve with an optimized nozzle design and with higher mass flow rates of HTF. The former, can be achieved with the utilization of design tools and numerical simulations while the latter calls for elimination of emulsification by mechanical or chemical means.
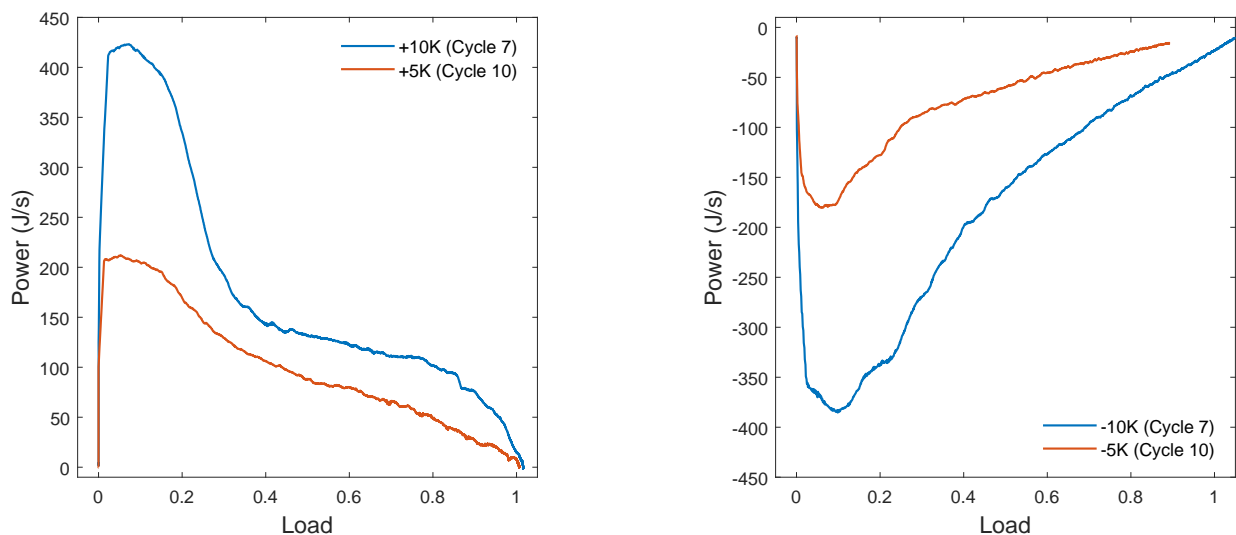

Figure 14. The power ($\dot{Q}_{charge}$) of Cycle 7 and Cycle 10 is shown over the load in order to compare the processes. Melting is shown on the left while solidification is shown on the right.

5. Additional Noteworthy Observations

Biofouling, seen in Figure 15, was a challenge for the presented setup and comprises an important challenge to be tackled in order to reach stable performance in direct contact systems.

A film of fungi, bacteria or remanence of a growing colony accumulated at the interface between the HTF and the PCM. The biomass adhered to the walls of the glass tube and spread out within the bulk emulsion when a HTF mass flow was started. A substantial biomass volume increase was observed whenever the system was running in a liquid–liquid configuration for extended periods of time. It is not clear whether the increase in biomass volume is due to growth of the colony or simply the visual result of the biomass being spread out over a larger area. When compared to a previous in-house direct contact system containing the material combination of TBAB (Tetra-n-butylammonium bromide) as PCM and D12 thermal oil as HTF, the biofouling was relatively mild. It is considered likely that the form in which the PCM is "stored" in the direct contact system (liquid or solid) plays a major role in bio growth acceleration. As the methyl palmitate was kept in solid form when the system was not in use (methyl palmitate has a melting temperature above the present ambient conditions) the growth rate was significantly smaller than with the TBAB which has a lower melting temperature. The biofilm influenced the emulsion growth and size by wrapping around and stabilizing the emulsion at the PCM–HTF interface.

Figure 15 shows the biological contamination in the system: without HTF flow on the left, at 15 kg h^{-1} in center and at 20 kg h^{-1} on the right. In the images that depict a mass flow through the biofilm, HTF "bubbles" covered by the contamination are clearly visible. This type of biofouling is assumed to have an influence on the emulsion buildup. The cleaning process described in the methodology section resulted in prolonging the time without major biocontamination. However, small amounts of biofouling usually appeared within a day of the PCM having been added to the system despite the system having been cleaned thoroughly beforehand. Utilization of suitable biocides could suppress the growth of bacteria and fungi in the system. However, biocides are hazardous substances that don't constitute a sustainable solution for this challenge. Alternatively, the development of suitable anti-biofouling coatings can be considered which would be a more environmentally friendly solution [57].
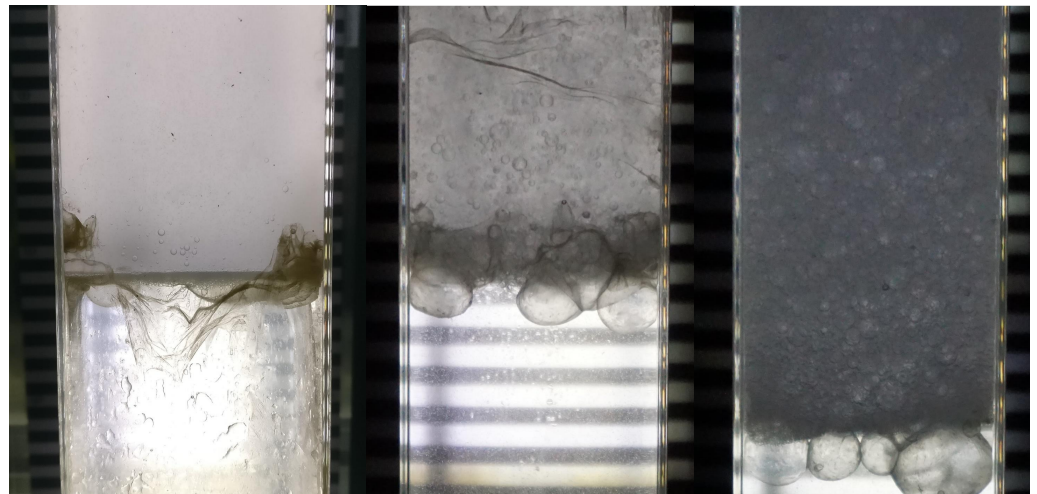

Figure 15. Images of biological contamination in the storage with: no HTF mass flow on the left, 15 kg h^{-1} and 20 kg h^{-1} in centre and on the right respectively.

6. Conclusions

In this study, a proof-of-concept setup using methyl palmitate as PCM and water as HTF was investigated in a DC-LHS context. Several melting/solidification cycles, as well as a multitude of operability experiments, were carried out under different experimental conditions. If some important, observed limitations can be surpassed, the concept presented could result in a simple, compact, cheap and sustainable solution for decentralized energy storage in the context of the energy turnaround.

Based on the presented experiments, methyl palmitate was found to be a suitable PCM option for direct contact latent heat storage when used in combination with water as HTF. No reaction between the PCM and HTF took place over the time that the system was active. The possibility of using water as HTF in DC-LHS, offers the potential to achieve a complete system with low environmental impact and low cost. Additionally, water is less corrosive and has approximately double the specific heat capacity of other HTF such as thermal oil, which is a HTF often used in DC-LHS setups. The large specific heat capacity allows for a sizable enthalpy flow even at low HTF mass flow rates. The operational stability of the system was only partially given. The HTF was able to find ways through the solidified PCM structure. Blockages inside the storage tank (glass tube) were never an issue when the PCM was solidified with a HTF flow present. Additionally, full charging and discharging could be demonstrated for all presented cycles, albeit with a high degree of uncertainty due to the nature of the system. The setup showed reproducible power when being melted and solidified. A high sensitivity to nozzle design and HTF inlet temperature was determined. Despite the system being unoptimized, all melting and solidification processes lasted less than one hour. This shows the potential for a good heat transfer performance if the system

were further improved (e.g., optimizing nozzle design and allowing higher HTF mass flow rates).

Two major challenges were observed in the investigated system which have been previously reported (albeit not in great detail). If the direct contact technology is to be successfully implemented in the future, these two obstacles must be overcome: (1) an emulsion that occurs when the system is in the liquid state that may lead to substantial PCM carry-over from the storage container into the rest of the system, (2) biological growth inside the storage container. Both of these phenomena limit the system performance (e.g., maximum mass flow rate) and affect the system stability in a way that would prevent the system from attaining the reasonable life-time of several years. In the authors' opinion both issues should be solved before further design optimization is pursued. For the emulsification issue, the option of using bio-based demulsifiers could be investigated. The biofouling could be addressed with the use anti-biofouling coatings which would be a more environmentally friendly solution than conventional biocides.

Author Contributions: All authors listed conceived and designed the project and contributed to experiments' development and in reviewing the paper; A.S. and J.W. acquired the funding; S.K., L.H. and D.F. designed and built the setup; L.H., R.R. and D.F. performed the experiments; L.H., R.R., S.K. and A.S. analyzed the data; L.H. wrote the paper. All authors have read and agreed to the published version of the manuscript.

Conflicts of Interest: The authors declare no conflict of interest.

Nomenclature

LHS	Latent Heat Storage
TES	Thermal Energy Storage
PV	Photovoltaic
DC-LHS	Direct Contact-Latent Heat Storage
PCM	Phase Change Material
HTF	Heat Transfer Fluid
ρ	Density ($\mathrm{kg\,m^{-3}}$)
c_p	Specific heat capacity
h_{melt}	Specific melting enthalpy
T_{in}	Inlet temperature
T_{out}	Outlet temperature
$\dot{m}_{htf}$	HTF mass flow rate
$\dot{H}_{htf}$	Enthalpy stream
$\dot{Q}_{loss}$	Heat losses to surroundings
T_{system}	System temperature
$T_{ambient}$	Ambient temperature
$\dot{Q}_{charge}$	Heat storing rate
Q_{max}	Heat storage capacity
m_{pcm}	Mass of PCM in the system
m_{glass}	Mass of glass tube
$T_{out}(end)$	Outlet temperature at the end of a process
$T_{out}(begin)$	Outlet temperature at the beginning of a process
$\Delta T_{in,out}$	Temperature difference between inlet and outlet
Q^*_{max}	Theoretical heat storage capacity
ΔT	Theoretical change in system temperature

References

1. Gur, I.; Sawyer, K.; Prasher, R. Searching for a better thermal battery. *Science* **2012**, *335*, 1454–1455. [CrossRef] [PubMed]
2. Kang, D.H.P.; Chen, M.; Ogunseitan, O.A. Potential environmental and human health impacts of rechargeable lithium batteries in electronic waste. *Environ. Sci. Technol.* **2013**, *47*, 5495–5503. [CrossRef] [PubMed]
3. Winslow, K.M.; Laux, S.J.; Townsend, T.G. A review on the growing concern and potential management strategies of waste lithium-ion batteries. *Resour. Conserv. Recycl.* **2018**, *129*, 263–277. [CrossRef]
4. Nazir, H.; Batool, M.; Bolivar Osorio, F.J.; Isaza-Ruiz, M.; Xu, X.; Vignarooban, K.; Phelan, P.; Inamuddin; Kannan, A.M. Recent developments in phase change materials for energy storage applications: A review. *Int. J. Heat Mass Transf.* **2019**, *129*, 491–523. [CrossRef]
5. Oró, E.; de Gracia, A.; Castell, A.; Farid, M.M.; Cabeza, L.F. Review on phase change materials (PCMs) for cold thermal energy storage applications. *Appl. Energy* **2012**, *99*, 513–533. [CrossRef]
6. Sharma, A.; Tyagi, V.; Chen, C.; Buddhi, D. Review on thermal energy storage with phase change materials and applications. *Renew. Sustain. Energy Rev.* **2009**, *13*, 318–345. [CrossRef]
7. Pereira da Cunha, J.; Eames, P. Thermal energy storage for low and medium temperature applications using phase change materials—A review. *Appl. Energy* **2016**, *177*, 227–238. [CrossRef]
8. Pielichowska, K.; Pielichowski, K. Phase change materials for thermal energy storage. *Prog. Mater. Sci.* **2014**, *65*, 67–123. [CrossRef]
9. Zhou, D.; Zhao, C.Y.; Tian, Y. Review on thermal energy storage with phase change materials (PCMs) in building applications. *Appl. Energy* **2012**, *92*, 593–605. [CrossRef]
10. Kalnæs, S.E.; Jelle, B.P. Phase change materials and products for building applications: A state-of-the-art review and future research opportunities. *Energy Build.* **2015**, *94*, 150–176. [CrossRef]
11. Stropnik, R.; Koželj, R.; Zavrl, E.; Stritih, U. Improved thermal energy storage for nearly zero energy buildings with PCM integration. *Sol. Energy* **2019**, *190*, 420–426. [CrossRef]
12. Cabeza, L.F.; Castell, A.; Barreneche, C.; De Gracia, A.; Fernández, A.I. Materials used as PCM in thermal energy storage in buildings: A review. *Renew. Sustain. Energy Rev.* **2011**, *15*, 1675–1695. [CrossRef]
13. Maranda, S.; Sponagle, B.; Worlitschek, J.; Groulx, D. Experimental Investigation of Thin PCM Packages and Thermal Spreader for Thermal Management of Portable Electronic Devices. *Appl. Sci.* **2019**, *9*, 4613. [CrossRef]
14. Landini, S.; Waser, R.; Stamatiou, A.; Ravotti, R.; Worlitschek, J.; O'Donovan, T.S. Passive cooling of Li-Ion cells with direct-metal-laser-sintered aluminium heat exchangers filled with phase change materials. *Appl. Therm. Eng.* **2020**, *173*, 115238. [CrossRef]
15. Agyenim, F.; Hewitt, N.; Eames, P.; Smyth, M. A review of materials, heat transfer and phase change problem formulation for latent heat thermal energy storage systems (LHTESS). *Renew. Sustain. Energy Rev.* **2010**, *14*, 615–628. [CrossRef]
16. Waser, R.; Maranda, S.; Stamatiou, A.; Zaglio, M.; Worlitschek, J. Modeling of solidification including supercooling effects in a fin-tube heat exchanger based latent heat storage. *Sol. Energy* **2020**, *200*, 10–21. [CrossRef]
17. Sheikholeslami, M.; Haq, R.u.; Shafee, A.; Li, Z. Heat transfer behavior of nanoparticle enhanced PCM solidification through an enclosure with V shaped fins. *Int. J. Heat Mass Transf.* **2019**, *130*, 1322–1342. [CrossRef]
18. Xiong, C.W.; Hu, J.Y.; Liu, X.L. *The Design of Variant Gradient Fractal Dot Matrix Structure Strengthening PCM Heat Sink*; Lecture Notes in Electrical Engineering; Springer: Berlin/Heidelberg, Germany, 2020; Volume 589, pp. 595–602.
19. Xie, J.; Choo, K.F.; Xiang, J.; Lee, H.M. Characterization of natural convection in a PCM-based heat sink with novel conductive structures. *Int. Commun. Heat Mass Transf.* **2019**, *108*, 104306. [CrossRef]
20. Saydam, V.; Parsazadeh, M.; Radeef, M.; Duan, X. Design and experimental analysis of a helical coil phase change heat exchanger for thermal energy storage. *J. Energy Storage* **2019**, *21*, 9–17. [CrossRef]
21. Mehling, H.; Cabeza, L.F. *Heat and Cold Storage with PCM*; Springer: Berlin/Heidelberg, Germany, 2008; pp. 11–55.
22. Martin, V.; He, B.; Setterwall, F. Direct contact PCM-water cold storage. *Appl. Energy* **2010**, *87*, 2652–2659. [CrossRef]
23. Nogami, H.; Ikeuchi, K.; Sato, K. Fundamental Flow Characteristics in a Small Columnar Latent Heat Storage Bath. *ISIJ Int.* **2010**, *50*, 1270–1275. [CrossRef]
24. Kunkel, S.; Teumer, T.; Dörnhofer, P.; Schlachter, K.; Weldeslasie, Y.; Kühr, M.; Rädle, M.; Repke, J.U. Determination of heat transfer coefficients in direct contact latent heat storage systems. *Appl. Therm. Eng.* **2018**, *145*, 71–79. [CrossRef]
25. Krimmel, S.; Stamatiou, A.; Worlitschek, J.; Walter, H. Experimental Characterization of the Heat Transfer in a Latent Direct Contact Thermal Energy Storage with One Nozzle in Labor Scale. *Int. J. Mech. Eng. Technol.* **2018**, *3*, 83–97.
26. Nomura, T.; Tsubota, M.; Okinaka, N.; Akiyama, T. Improvement on heat release performance of direct-contact heat exchanger using phase change material for recovery of low temperature exhaust heat. *ISIJ Int.* **2015**, *55*, 441–447. [CrossRef]
27. Gao, L.; Zhao, J.; An, Q.; Zhao, D.; Meng, F.; Liu, X. Experiments on thermal performance of erythritol/expanded graphite in a direct contact thermal energy storage container. *Appl. Therm. Eng.* **2017**, *113*, 858–866. [CrossRef]
28. Kiatsiriroat, T.; Vithayasai, S.; Vorayos, N.; Nuntaphan, A.; Vorayos, N. Heat transfer prediction for a direct contact ice thermal energy storage. *Energy Convers. Manag.* **2003**, *44*, 497–508. [CrossRef]
29. Farid, M.M.; Khudhair, A.M.; Razack, S.A.K.; Al-Hallaj, S. A review on phase change energy storage: Materials and applications. *Energy Convers. Manag.* **2004**, *45*, 1597–1615. [CrossRef]

30. Kaizawa, A.; Kamano, H.; Kawai, A.; Jozuka, T.; Senda, T.; Maruoka, N.; Akiyama, T. Thermal and flow behaviors in heat transportation container using phase change material. *Energy Convers. Manag.* **2008**, *49*, 698–706. [CrossRef]

31. Ravotti, R.; Fellmann, O.; Lardon, N.; Fischer, L.; Stamatiou, A.; Worlitschek, J. Synthesis and Investigation of Thermal Properties of Highly Pure Carboxylic Fatty Esters to Be Used as PCM. *Appl. Sci.* **2018**, *8*, 1069. [CrossRef]

32. Riemenschneider, W.; Bolt, H.M. Esters, Organic. In *Ullmann's Encyclopedia of Industrial Chemistry*; Wiley: Hoboken, NJ, USA, 2005.

33. Buddrus, J.; Schmidt, B. *Grundlagen der Organischen Chemie*; De Gruyter: Berlin, Germany; München, Germany; Boston, MA, USA, 2015.

34. Noël, J.A.; Allred, P.M.; White, M.A. Life cycle assessment of two biologically produced phase change materials and their related products. *Int. J. Life Cycle Assess.* **2015**, *20*, 367–376. [CrossRef]

35. Feldman, D.; Banu, D.; Hawes, D. Low chain esters of stearic acid as phase change materials for thermal energy storage in buildings. *Sol. Energy Mater. Sol. Cells* **1995**, *36*, 311–322. [CrossRef]

36. Ravotti, R.; Fellmann, O.; Fischer, L.J.; Worlitschek, J.; Stamatiou, A. Investigation of the thermal properties of diesters from methanol, 1-pentanol, and 1-decanol as sustainable phase change materials. *Materials* **2020**, *13*, 810. [CrossRef] [PubMed]

37. Ravotti, R.; Fellmann, O.; Lardon, N.; Fischer, L.J.; Stamatiou, A.; Worlitschek, J. Analysis of bio-based fatty esters PCM's thermal properties and investigation of trends in relation to chemical structures. *Appl. Sci.* **2019**, *9*, 225. [CrossRef]

38. Noël, J.A.; Kahwaji, S.; White, M.A. Molecular structure and melting: implications for phase change materials. *Can. J. Chem.* **2018**, *96*, 722–729. [CrossRef]

39. Karaipekli, A.; Sari, A. Preparation and characterization of fatty acid ester/building material composites for thermal energy storage in buildings. *Energy Build.* **2011**, *43*, 311–322. [CrossRef]

40. Stamatiou, A.; Obermeyer, M.; Fischer, L.J.; Schuetz, P.; Worlitschek, J. Investigation of unbranched, saturated, carboxylic esters as phase change materials. *Renew. Energy* **2017**, *108*, 401–409. [CrossRef]

41. Alper Aydn, A. High-chain fatty acid esters of 1-octadecanol as novel organic phase change materials and mathematical correlations for estimating the thermal properties of higher fatty acid esters' homologous series. *Sol. Energy Mater. Sol. Cells* **2013**, *113*, 44–51. [CrossRef]

42. Aydn, A.A.; Okutan, H. High-chain fatty acid esters of myristyl alcohol with odd carbon number: Novel organic phase change materials for thermal energy storage—2. *Sol. Energy Mater. Sol. Cells* **2011**, *95*, 2417–2423. [CrossRef]

43. Rafin, C.; Veignie, E. Hormoconis resinae, The Kerosene Fungus 16. In *Taxonomy, Genomics and Ecophysiology of Hydrocarbon-Degrading Microbes*; Springer: Berlin/Heidelberg, Germany, 2019.

44. Edie, D.D.; Melsheimer, S.S.; Mullins, J.C. *Immiscible Fluid-Heat of Fusion Heat Storage System*; Technical Report; NASA: Washington, DC, USA, 1979.

45. Horibe, A.; Jang, H.; Haruki, N.; Sano, Y.; Kanbara, H.; Takahashi, K. Melting and solidification heat transfer characteristics of phase change material in a latent heat storage vessel: Effect of perforated partition plate. *Int. J. Heat Mass Transf.* **2015**, *82*, 259–266. [CrossRef]

46. Kaizawa, A.; Maruoka, N.; Kawai, A.; Kamano, H.; Jozuka, T.; Senda, T.; Akiyama, T. Thermophysical and heat transfer properties of phase change material candidate for waste heat transportation system. *Heat Mass Transf./Waerme- Stoffuebertragung* **2008**, *44*, 763–769. [CrossRef]

47. Ammann, S.; Ammann, A.; Ravotti, R.; Fischer, L.J.; Stamatiou, A.; Worlitschek, J. Effective separation of awater in oil emulsion from a direct contact latent heat storage system. *Energies* **2018**, *11*, 2264. [CrossRef]

48. Naing, T.T.; Horibe, A.; Haruki, N.; Yamada, Y. *Reduction of the Solidification Height of Phase-Change Material in Direct-Contact Latent Heat Storage Vessel*; Technical Report 1; Yangon Technological University: Yangon, Myanmar, 2018.

49. Hartland, S.; Jeelani, S.A. Choice of model for predicting the dispersion height in liquid/liquid gravity settlers from batch settling data. *Chem. Eng. Sci.* **1987**, *42*, 1927–1938. [CrossRef]

50. Henschke, M.; Schlieper, L.H.; Pfennig, A. Determination of a coalescence parameter from batch-settling experiments. *Chem. Eng. J.* **2002**, *85*, 369–378. [CrossRef]

51. Hartland, S.; Jeelani, S.A. Prediction of sedimentation and coalescence profiles in a decaying batch dispersion. *Chem. Eng. Sci.* **1988**, *43*, 2421–2429. [CrossRef]

52. Martin-Sanchez, P.M.; Gorbushina, A.A.; Toepel, J. Quantification of microbial load in diesel storage tanks using culture- and qPCR-based approaches. *Int. Biodeterior. Biodegrad.* **2018**, *126*, 216–223. [CrossRef]

53. Shkilniuk, I.; Boichenko, S.; Kondratiuk, T.; Shevchuk, N. *Identification and Assessment of Biological Risk of Aviation Fuel Supply*; National Aviation University: Kyiv, Ukraine, 2019.

54. Melanie, N. *Thermal Analysis Tips and Hints*; Cardiff University: Cardiff, UK, 2016; Volume 2.

55. DURAN Group. *Materialdatenblatt/Spezifikation DURAN ® Glas*; Technical Report; DURAN Group: Wertheim am Main, Germany, 2014.

56. Weingärtner, H.; Teermann, I.; Borchers, U.; Balsaa, P.; Lutze, H.V.; Schmidt, T.C.; Franck, E.U.; Wiegand, G.; Dahmen, N.; Schwedt, G.; et al. Water, 1. Properties, Analysis, and Hydrological Cycle. In *Ullmann's Encyclopedia of Industrial Chemistry*; Wiley-VCH Verlag GmbH & Co. KGaA: Weinheim, Germany, 2016; pp. 1–40.

57. Callow, J.A.; Callow, M.E. Trends in the development of environmentally friendly fouling-resistant marine coatings. *Nat. Commun.* **2011**, *2*, 244. [CrossRef]